Applied Ocean Research 173 (2026) 105174

Contents lists available at ScienceDirect

Applied Ocean Research

journal homepage: www.elsevier.com/locate/apor

Research paper

Horizontal-axis tidal turbine array simulation based on blade-section model (BSM) in two-dimensional space

Morhaf Aljber [a,*], Han Soo Lee [a,b,c,*]

[a] Coastal Hazards and Energy System Science Laboratory, Graduate School of Innovation and Practice for Smart Society, Hiroshima University, 1-5-1 Kagamiyama, Higashi-Hiroshima, 739-8529, Hiroshima, Japan

[b] Center for Planetary Health and Innovation Science (PHIS), The IDEC Institute, Hiroshima University

[c] Transdisciplinary Science and Engineering Program, Graduate School of Advanced Science and Engineering, Hiroshima University

ARTICLE INFO

Keywords:
Horizontal-axis tidal turbine
Turbulent wake characteristics
Navier Stokes equation
Adaptive mesh refinement
Blade section model
Basilisk open solver

ABSTRACT

Understanding the hydrodynamic interactions within tidal arrays is essential for designing turbine alignment and optimising power output. While three-dimensional simulations offer detailed insight into wake dynamics and velocity recovery, their computational cost is a main challenge, especially for large-scale farm designs. This study introduces a novel two-dimensional concept to simulate a tidal turbine based on turbine blade section modelling (BSM) as a representative of the entire rotor. The model integrates the Navier–Stokes (NS) solver-based Basilisk open source with adaptive mesh refinement (AMR) and embedded boundary conditions (EBC). The NS-BSM method was validated against physical flume experiments and numerical results. Several farm layouts with one, two, and three rows of turbines were tested. The NS-BSM achieves a balance between computational efficiency and physical realism, enabling rapid assessment of turbine-induced flow dynamics. The simulations were conducted in parallel using 48 CPUs, with 100 s of flow evolution completed at approximately 6 min. The NS-BSM accurately produced complicated flow patterns and velocity deficits in the near- and far-wake regions accurately. However, this approach does not resolve vertical flow dynamics, limiting its applicability for evaluating wave–current interactions, seabed scouring, and detailed loading on turbine blades or support structures. Despite these limitations, the NS-BSM serves as a practical tool for scenario-based tidal farm optimisation, significantly reducing computational demand while maintaining high accuracy.

1. Introduction

Marine renewable energy (MRE) is gaining momentum as a vital contributor to the global sustainable energy transition (Hasselman et al., 2023). The rapid development of MREs presents both promising opportunities and significant challenges (Li et al., 2022). In recent years, the exclusive economic zones (EEZs) of many countries have become focal points for investment, particularly offshore wind and solar farms (Cheynet et al., 2024; Díaz and Guedes Soares, 2020; Ramanan et al., 2024). Within this expanding landscape, tidal stream energy (TSE) stands out as a consistent and predictable resource. The commercialisation of tidal turbines has accelerated the adoption of TSEs with active projects in the UK, Japan, France, and South Korea (Bae et al., 2010; Claire Cohen and Tim Baker, 2020; Kyuden Mirai Ltd, 2025; Ocean Energy Europe, 2025). Energetic tidal sites where current velocities exceed 2 m/s with high frequency occurrence offer a sustainable energy source at competitive costs, especially if full exploitation is realised (Aljber et al., 2025, 2024a, 2023).

Tidal farms are essential for achieving cost-effective power generation. By leveraging economies of volume, the deployment of larger farms reduces unit capital and operational expenditures through supply chain scaling and repeatable construction and maintenance processes (Aljber

Abbreviations: ADCP, Acoustic doppler current Profile; ALM, Actuator line method; AMR, Adaptive mesh refinement; B, Bias; BEM, Blade element momentum; BSM, Blade section model; CFD, Computational fluid dynamics; CFL, Courant Friedrichs Lewy; CPU, Central processing unit; D, Turbine diameter; DNS, Direct numerical simulation; EBC, Embedded boundary conditions; EEZs, Exclusive economic zones; EMEC, European marine energy centre; GPS, Global positioning system; HPC, High performance computing; LES, Large eddy simulation; LBM, Lattice Boltzmann method; MRE, Marine renewable energy; NACA, National advisory committee for aeronautics; NS, Navier Stokes; PDF, Probability density function; RANS, Reynolds averaged Navier Stokes; RMSE, Root means square error; TI, Turbulence intensity; TSE, Tidal stream energy; VOF, Volume of fluid.

* Corresponding authors.
E-mail addresses: morhafaljber@gmail.com (M. Aljber), leehs@hiroshima-u.ac.jp (H.S. Lee).

https://doi.org/10.1016/j.apor.2026.105174
Received 14 March 2026; Received in revised form 24 June 2026; Accepted 8 July 2026
Available online 13 July 2026

et al., 2025; Arup, 2016; Smart and Noonan, 2018). However, farm-scale deployment affects local flow dynamics by introducing additional turbulence and reducing downstream tidal velocities. The available flow velocity at the downstream rows is a key factor in determining the overall power extraction efficiency. Hydrodynamic analysis of tidal turbine arrays is essential for optimising turbine placement and maximising power extraction. Lessons from early wind energy development are highly relevant to TSEs, particularly with respect to wake interactions. Insufficient attention to momentum recovery and wake influence in the Horns Rev Offshore wind farm led to a 40% reduction in downstream turbines compared with front-row turbines (Mehta et al., 2014). This underscores the need for integrated wake considerations in tidal farm design. At candidate tidal sites, the available space for farm deployment is often constrained by the limited extent of high-velocity zones, avoiding conflicts of interest between stakeholders and the presence of environmentally protected areas, fisheries, or aquaculture zones (Aljber et al., 2024a; Philip Marsh et al., 2021; Marsh et al., 2021b). Therefore, tidal farms must operate efficiently within these spatial constraints, necessitating careful optimisation of array spacing.

Experimental studies have been conducted to quantify the flow dynamics in the wakes of tidal turbines. The wake recovery distance is a critical factor in determining the optimal position of downstream turbine rows. According to Gaurier et al. (2020), the wake recovery is faster in a highly turbulent zone, which is favourable for increasing the turbine density on the farm. Lateral spacing is typically determined by evaluating the lateral expansion of the wake. Typically, the wake exhibits slight asymmetry about the rotor centreline, which is influenced by flow vorticity and shear. The vortex intensity of the flow decreases in the near-wake region and reaches a nearly constant value far downstream (Zhang et al., 2021). Accordingly, some studies have suggested that a confined tidal array benefits from the blockage effect, which is achieved by minimising the lateral distance between rows (Liu et al., 2025; McAdam et al., 2013). Field surveys using acoustic Doppler current profilers (ADCPs) have been conducted to characterise the flow regime downstream of pilot tidal turbines in the UK, Canada, and Japan (Garcia-Novo et al., 2024; Guerra and Hay, 2024; Lieber et al., 2024). These studies consistently reported that velocity recovery occurs approximately 5–10 times the turbine diameter (D) downstream, depending on the turbine configuration and local flow conditions. ADCPs were deployed either on (global positioning system) GPS-tracked drifters or vessel-mounted systems to collect velocity profiles along and across the turbine wake. Flow recovery was assessed by comparing velocity measurements within the wake zone to those in the ambient undisturbed flow. Despite valuable insights from experimental studies and field surveillance, expensive equipment and time consumption are major barriers. Furthermore, the absence of fully commissioned tidal farms limits information about full-scale farm-induced flow dynamics.

Three-dimensional numerical models have been widely used to investigate the flow dynamics and performance of single tidal turbines. Studies have employed Reynolds-averaged Navier–Stokes (RANS) simulations to evaluate turbine behavior under different flow conditions (Mohammadi and GKnight, 2025; Song et al., 2020). While RANS offers moderate accuracy with low computational cost, large eddy simulation (LES) provides more detailed insights at higher computational demand. LES, coupled with embedded boundary conditions (EBC), has been used to study the hydrodynamics and loading of a single tidal turbine, showing that increased ambient turbulence accelerates wake recovery and amplifies unsteady blade loads by up to 50% (Ouro et al., 2017). Wang et al. (2020) and Zhang et al. (2022) highlighted the importance of fluid–structure interaction (FSI) methods for capturing blade deformation and wake structure, which cannot be captured by computational fluid dynamics (CFD) methods. Ahmed et al. (2017) reported that under low-turbulence conditions, RANS and LES yield similar phase-averaged loads and pressures. However, only the LES with synthetic inflow turbulence accurately captures the full frequency range of bending moment fluctuations. Geometry-resolved LES also reveals flow features near the turbine that are difficult to observe experimentally, highlighting its value for detailed load analysis and device optimisation. This high accuracy was also confirmed by Ouro et al. (2024) and Posa et al. (2024) in quantifying the effects of waves and the tip speed ratio on wake recovery.

While three-dimensional LES offers high accuracy for single turbines, their substantial computational demands make them challenging for full tidal farm simulations, especially when coupled with EBC. To reduce costs, three-dimensional RANS models have been used effectively to simulate farm-induced wakes, such as for vertical-axis tidal turbines, by averaging the force coefficients on three-dimensional blades (Gauvin-Tremblay and Dumas, 2022). Other approaches have combined the actuator line method (ALM) with the lattice Boltzmann method (LBM) to model farms (Watanabe and Hu, 2022). Nuernberg and Tao (2018) applied three-dimensional RANS in OpenFOAM to study farm-scale flow and wake dynamics. They noted that further refinement is needed to resolve wake features accurately.

Simplified two-dimensional LES models with adaptive mesh refinement (AMR) have also been used to optimise the array spacing and power output, treating turbines as zones of enhanced bottom friction (Divett et al., 2016, 2013). Wallwork et al. (2024) applied goal-oriented mesh adaptation to a shallow-water tidal farm model, achieving array energy estimates within 2% of a high-resolution mesh. However, these models omit rotor-induced vorticity and underestimate downstream turbulence. Xu et al. (2025) proposed a mesh-based data-driven framework coupled with neural networks to predict the hydrodynamic performance of tidal turbine blades and maximise the power coefficient. A more balanced approach couples three-dimensional LES with the ALM, resolving full-scale wake behavior more accurately (Ouro et al., 2019; Ouro and Nishino, 2021). However, this accuracy accounts for the tremendous computational demand.

High accuracy clearly accounts for large computational demands. Therefore, in this study, a novel concept was proposed to model tidal turbines and quantify the downstream velocity by providing a compromise of high accuracy and low computational cost. The tidal turbine is modelled on the basis of the blade cross section as the effective part for vorticity-induced flow dynamics. The model adopts the cross section of the blades to present the full turbine rotor in a two-dimensional domain. A simulation was conducted using the Navier Stokes solver in the Basilisk open-source flow solver with AMR and EBC. The model was validated with experimental and numerical results and demonstrated high fidelity in reproducing the downstream velocity fluctuations and turbulence intensity for different tidal farm layouts.

The paper is divided into seven sections. The first section is the introduction. The concept of the blade section model is described in Section 2. Section 3 presents the experimental studies that were used for validation, and the methods are described in Section 4. The results are presented in Section 5, followed by a discussion and conclusions in Sections 6 and 7, respectively.

2. Rationale of the blade section model (BSM)

The turbine extends in three-dimensional space and rotates in two-dimensional space, such as the X-Z plane, while the flow is moving in the Y-Z plane (Fig. 1). Within the X-Z plane, the rotor occupies an area determined by the rotor diameter, while the flow interacts with the blades to generate rotation. The pitch angle (the angle between the blade chord line and the rotational plane) of the blade determines the effective cross section that receives the flow, and the angle of attack (the angle between the blade chord line and the relative flow vector) determines the forces applied on the cross section. The tidal turbine defined by the blade sections is shown in Fig. 1(b). The flow interacts with the blade to generate rotation, as depicted in Fig. 1(c), and continues to develop into a wake downstream. The lateral expansion of the wake in the crosswise direction is proportional to the rotor area. Therefore, the wake downstream is induced mainly by the blade section

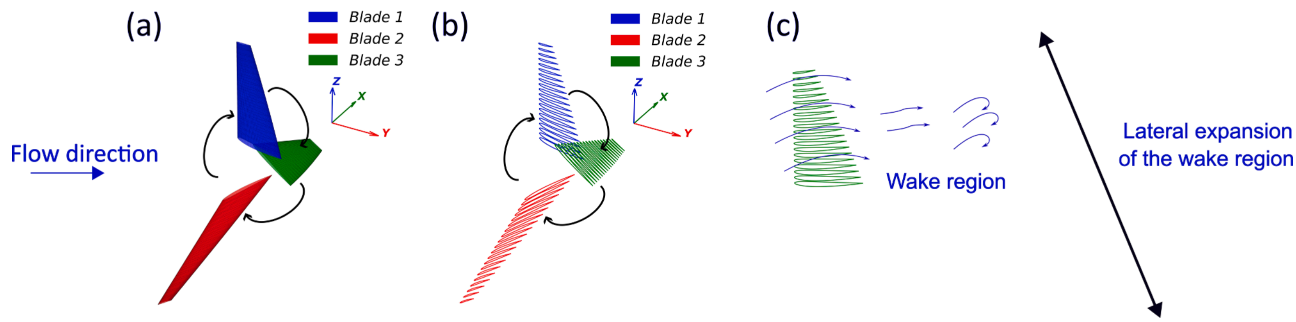

Fig. 1. Turbine flow interplay analysis. (a) Full rotor blades in three-dimensional mode without the nacelle, (b) the rotor blades presented by the blade cross-section, and (c) the wake generation downstream due to the interaction between the flow trajectories and the blade.

and the rotation of the rotor. Hence, the hypothesis of this study is how to reproduce the flow-blade interplay accurately with minimum computational demand. Both the blade element momentum (BEM) theory and the ALM estimate the hydrodynamic forces acting on blade cross-sections, but they differ fundamentally in how these forces interact with the flow. The BEM divides the rotor into independent radial sections and determines the sectional forces by enforcing the conservation of axial and angular momentum within each radial section, without explicitly resolving the surrounding flow field (Masters et al., 2011; Ning et al., 2015). In contrast, the ALM computes sectional lift and drag forces and distributes them into the computational domain as spatially distributed body forces acting on the fluid (Baba-Ahmadi and Dong, 2017; Sorensen et al., 2015). This procedure represents the rotating blades within a three-dimensional flow simulation, allowing the turbine–wake interaction to develop dynamically. In both approaches, the magnitude of the force depends on the local blade section geometry and hydrodynamic characteristics.

Thus, instead of conducting a two-way force–flow calculation, the blade can be constructed directly in the model using the EBC. With this approach, no modification is required in the governing equation (the flow solver model). The second idea is that constructing the full rotor in a three-dimensional space is computationally expensive. To reduce the computational burden, only the effective part of the rotor, the blade cross section, can be constructed. Figure 2(a) illustrates how the cross-section of the blade functions during the operation of the tidal turbine illustrates how the cross-section of the blade functions during the operation of the tidal turbine. The flow vectors interact with the blade cross-section, generating the lift force that causes rotation, and then, the flow continues downstream, developing into the wake (Fig. 2(b)). The velocity deficit downstream is determined by the wake evolution. Therefore, the blade cross-section (effective part) is adequate to produce the correct physical interaction of the entire blade. To produce lateral wake expansion of the three blades, three cross sections were subsequently used in two-dimensional space. The relationship between the flow and turbine blades can be presented in a two-dimensional space, as shown in Fig. 2(c). Each blade is presented as a cross-section, and the chord of the cross-section is extended to replicate the rotor area within a two-dimensional (X-Y) plane. Theoretically, on the basis of the aforementioned discussion, the blade-section model (BSM) should accurately produce the turbine–flow interplay. To validate this hypothesis, a numerical simulation was conducted following the setting of a series of tidal flume experiments, and the results from the BSM model were hindcasted with the physical flume results and three-dimensional RANS-BEM results.

3. Tidal flume experiment

Hydrodynamic analysis of the turbine–flow interplay is key for determining the optimal layout of a tidal farm. It is known that rotor rotation generates wake downstream, and the tidal velocity is reduced. Identifying the structure and extension of the wake is key for identifying the recovery distance for the velocity and quantifying the power extraction from the tidal turbine. Stallard et al. (2013a, 2015) conducted a series of physical experiments in an open-channel flume that was 5 m wide, 12 m long, and 0.45 m deep. The flow velocity was 0.47 m/s. A porous weir was used to generate a 10–12% turbulence intensity. A turbine with a diameter of D = 0.27 m was installed at mid-depth, and the turbine rows started at X = 6 m from the turbulence generator. The experiment was performed at a scale of 1:70 featuring a 19 m diameter tidal turbine at an approximately 31.5 m water depth. The turbine used a three-bladed rotor, and the geometry was optimised to match the thrust and power characteristics of full-scale turbines at a tip speed ratio of 4.5. Each blade followed a Göttingen 804 profile. The rotor was fabricated as a single unit layer of glass fibre-reinforced polymer acrylic. The experiments were conducted for a row of three turbines with a lateral space of 1.5D Velocity measurements were taken downstream at 2D, 4D, 6D, 8D,

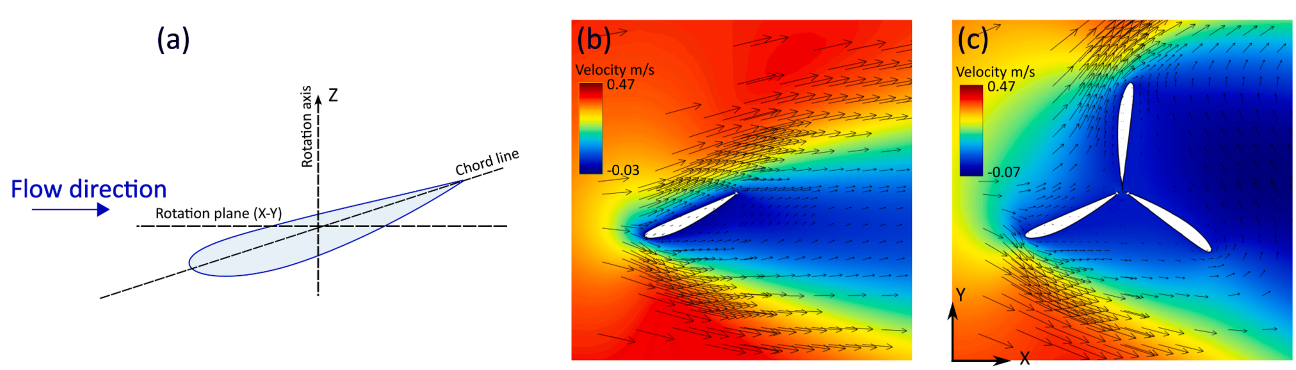

Fig. 2. Conceptualisation of the blade section model (BSM). (a) Analysis of the flow effect on the blade cross-section, (b) the interaction between the flow and the blade section along with velocity vectors in two-dimensional space, and (c) the representation of the tidal turbine using the hydrofoil blade section in two-dimensional space (X−Y plane).

10D, and 12D The turbulence intensity (TI) was subsequently calculated at the same positions to quantify the wake structures and integrate them with the ambient flow. The TI in Eq. (1) is the standard deviation of the speed (fluctuations) divided by the reference speed.

$$TI = \frac{\sqrt{(u - \overline{u})^2}}{u_0} \tag{1}$$

where u is the instant velocity, $\overline{u}$ is the mean velocity, and u_0 is the reference velocity (0.47 m/s).

The authors reported that the mean flow velocity for a single rotor decreases to approximately 20% of the incident velocity in the near wake at 1.5D and then recovers to 80% at approximately 10D downstream. These results agreed with the standard recommendation of longitudinal space between rows from the EMEC (European Marine Energy Centre Ltd., 2009). The highest TI, equal to 18%, was observed at 3D and then decreased to 10% at 10D For an array of three rotors, the individual wake was still identifiable at 6D. At 8D and beyond, the individual wakes merged into a single wake, and the velocity deficit exhibited negligible variation across the channel width. The TI was approximately constant after 8D, with minor variation from the ambient TI.

In Olczak et al. (2016), the flume experiment was expanded to assess an array with multiple rows. The experiments included array layouts of two rows with 4D and 8D longitudinal spaces, where the first row featured three turbines and the second row featured four turbines. An array of three rows with 4D longitudinal space where the rows feature three, four, and five turbines from upstream to downstream. The arrays adopted staggered turbine layouts, and the lateral space was 1.5D in all the experiments. Furthermore, the authors conducted a numerical simulation via coupled RANS with BEM theory. The results of the numerical simulation were validated with flume experiment results. The conceptual layout of the physical flume experiments is shown in Fig. 3. The authors of the aforementioned studies published experimental and numerical results (https://royalsocietypublishing.org/doi/suppl/10.1098/rsta.2012.0159) (DOI: 10.13140/RG.2.1.3842.6482), which were used to validate our results.

4. Method

4.1. Incompressible Navier Stokes solver with a cell-centered formulation

In this study, all the numerical simulations were conducted via the Basilisk open-source flow solver. The Basilisk solver is based on C language and solves the one-, two-, and three-dimensional partial differential equations on an adaptive cartesian mesh. For further information, Basilisk's official documentation is available online (Basilisk, 2025). The incompressible, variable-density, Navier–Stokes (NS) equation with cell-centred discretisation, *centered.h* library in Basilisk (Lagrée et al., 2011; Popinet, 2009, 2003), was utilised to conduct the numerical simulation in this study. The governing equations for the NS solver with an EBC are described as follows:

$$\rho(\partial_t \boldsymbol{u} + \boldsymbol{u} \cdot \nabla \boldsymbol{u}) = -\nabla p + \nabla \cdot (2\mu \boldsymbol{D}) \tag{2}$$

$$\nabla \cdot \boldsymbol{u} = 0 \tag{3}$$

where ρ is the fluid density, $\boldsymbol{u} = (u, v)$ is the velocity field in the x and y directions, p is the pressure field, μ is the dynamic viscosity, and $\boldsymbol{D} = (\partial_i v + \partial_j u)$ is the deformation tensor.

The NS scheme uses a generic time loop that is stable when the Courant-Friedrichs-Lewy (CFL) condition is less than one. The method is a second-order (in space and time) discretisation of the incompressible NS equations that implements the Bell–Collela–Glaz scheme for velocity advection (Bell et al., 1989) and a multigrid Poisson solver for pressure projection. In the centered NS solver, the pressure and velocity fields are computed through iterative loops. The predicted velocity field in the next time step $\boldsymbol{u}_*$ ($\boldsymbol{u}_* \approx \boldsymbol{u}_{n+1}$) is first computed via a time discretisation of Eq. (2) without considering the pressure term.

$$\rho_{n+\frac{1}{2}} \left[\frac{\boldsymbol{u}_* - \boldsymbol{u}_n}{\Delta t} + \boldsymbol{u}_{n+\frac{1}{2}} \cdot \nabla \boldsymbol{u}_{n+\frac{1}{2}} \right] = \nabla \cdot \mu_{n+\frac{1}{2}} (\boldsymbol{D}_n + \boldsymbol{D}_*) \tag{4}$$

Afterward, a pressure correction is computed by solving the Poisson equation for pressure.

$$\nabla \cdot \boldsymbol{u}_* = \nabla \cdot \left[\frac{\Delta t}{\rho_{n+\frac{1}{2}}} \nabla p_{n+\frac{1}{2}} \right] \tag{5}$$

The predicted velocity $\boldsymbol{u}_*$ is then corrected via the newly computed pressure field to obtain the final velocity field $\boldsymbol{u}_{n+1}$ at the next time step:

$$\boldsymbol{u}_{n+1} = \boldsymbol{u}_* - \frac{\Delta t}{\rho_{n+\frac{1}{2}}} \nabla p_{n+\frac{1}{2}} \tag{6}$$

This correction ensures that the final velocity field satisfies the

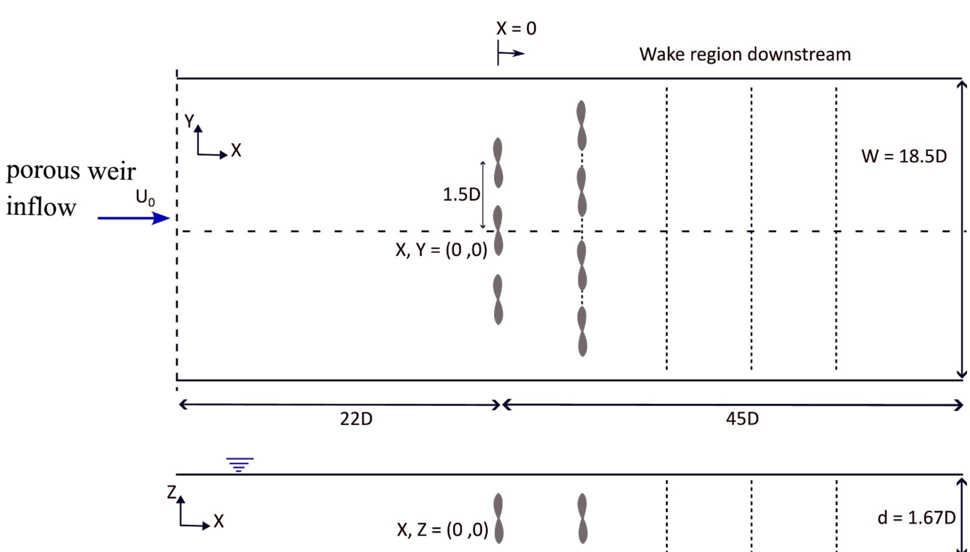

Fig. 3. General arrangement of the physical flume experiment layout by Olczak et al. (2016).

incompressibility condition. The boundary conditions (no-slip conditions) are identified beforehand at the embedded boundaries (turbines in this case).

4.2. Embedded boundary condition (EBC) with a volume of fluid (VOF) advection scheme

The embedded boundary is constructed starting from a uniform Cartesian grid Ω_Δ; then, it is generalised to a quadtree/octree AMR. For the simulation set-up, a distance function Φ was defined, which is the turbine geometry in this case (blade section). Afterward, a discrete piecewise continuous representation of the rigid boundary, Γ_Δ, is embedded in the grid Ω_Δ and intersects the underlying cells to form irregular fluid control volumes, V (Fig. 4(a), Fig. 4(b). The VOF quantities in the cut-cell, the volume fraction c and the area fraction f of the effective volume of the fluid. Note that the superscripts ^{f} and ^{v} in Fig. 4 (b) denote the cell face and vertex, respectively, following the Basilisk notation (Ghigo et al., 2023). In each cut-cell, the discrete rigid boundary $\delta\Gamma_\Delta$ satisfies Eq. (7) for a line:

$$\overline{n_\Gamma}\cdot x = \alpha \tag{7}$$

where $\overline{n_\Gamma}$ is the inwards unit normal vector to the discrete rigid boundary and where α is the intercept.

The interface in each cell is described via a piecewise-linear VOF scheme and is used to solve the advection equation. By assuming that the volume fraction c is bounded between zero and one, the interface position x_n is described by Eq. (8):

$$x_n = \begin{cases} x_{n-1/2} + c_i\Delta \ \mathit{for}\ 0 < c_i < 1 \\ \mathit{undefined\ otherwise} \end{cases} \tag{8}$$

Basilisk consists of field values in 3×3 structured neighbors, and stencils are employed to access these values. As defined in Fig. 4(b), the distance function Φ is sampled on the Cartesian grid edges. Therefore, the interface position is not defined when the volume fraction c is not bounded between zero and one.

Then, the flux $F_{n+1/2}$ is computed geometrically via the flow velocity u and the interface position x (Fig. 5), as described in Eq. (9):

$$F_{n+1/2} = \begin{cases} 0 \ \mathit{if}\ x_n + u_{n+\frac{1}{2}}\Delta t \ \le x_{n+1/2} \\ u_{n+1/2}\ \mathit{if}\ x_n \ge x_{n+1/2} \\ \frac{1}{\Delta t}\left(x_n + u_{n+\frac{1}{2}}\Delta t - x_{n+\frac{1}{2}}\right) \ \mathit{otherwise} \end{cases} \tag{9}$$

The height function determines the distance between the interface and the cell edge and can be defined along either the x- or y-coordinate.

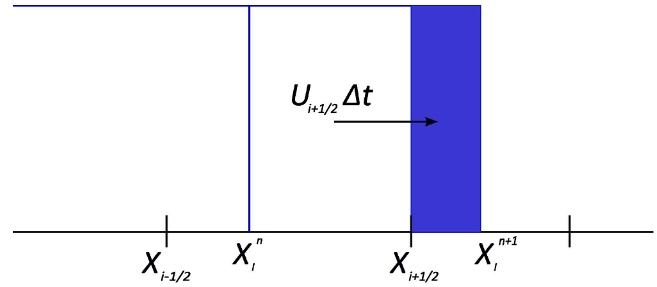

Fig. 5. The graphical advection scheme of the VOF method with the flux calculation $F_{n+1/2}$ (blue area) represented by the time-dependent velocity and Cartesian grid position for the embedded boundary (Popinet, 2011).

$$y = h(x) \tag{10}$$

or

$$x = h(y) \tag{11}$$

On a two-dimensional cartesian grid, the optimal stencil is aligned with the normal direction of the interface. For the AMR, a local asymmetric stencil adapted to the geometry of the interface is built. When the interface cannot be described by a vertical or horizontal line, the solution adapts a parabolic curve. For further reading, refer to (Ghigo et al., 2023; Limare et al., 2023; Popinet, 2018, 2011, 2009)

4.3. Adaptive mesh refinement (AMR)

The Basilisk framework employs an AMR system built on a tree-based Cartesian grid. This mesh is refined automatically, allowing the local resolution to increase where needed. The maximum and minimum refinement levels (2^8 and 2^5, respectively) are specified as part of the simulation setup, which is equal to approximately 0.09 m in the turbine and wake region and approximately 0.75 m in the undisturbed flow region. A grid independence study was conducted across three hierarchical AMR maximum refinements (2^7, 2^8, and 2^9). The turbine blade geometry was fixed at level 8 across all runs to isolate the sensitivity of the wake flow from geometric representation effects. The L_2 norm of the difference in the velocity deficit profile was used to quantify the convergence rate with higher resolution (Sabia et al., 2026). L_2 tracks the difference in the velocity deficit profile shape between two grid levels at a given station x and is defined as follows:

$$L_2 = \sqrt{\frac{1}{N}\sum_{j=1}^{N}\left(\Delta u_{\mathrm{Li}}\left(y_j\right) - \Delta u_{\mathrm{Li+1}}\left(y_j\right)\right)^2} \tag{12}$$

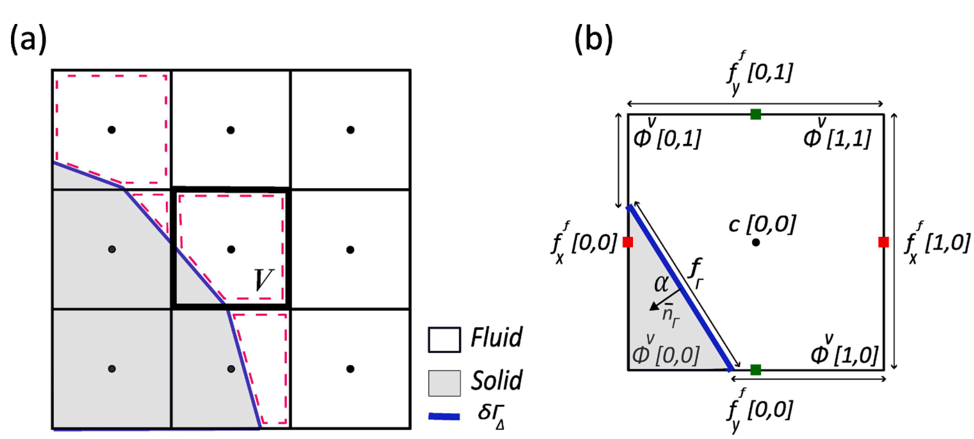

Fig. 4. (a) Two-dimensional representation of the Cartesian embedded boundary with cut cells by a solid irregular volume fraction defined by the rigid boundary $\delta\Gamma_\Delta$ and (b) the level-set representation of the cut-cell by the distance function Φ and the volume-of-fluid quantities (Ghigo et al., 2023).

where Δu_{Li} is the normalised velocity at x (X/D = 2, 4, 6, 8, 10, and 12) with level i sampled at discrete y-points and Δu_{Li+1} is the normalised velocity at the same location with level $i+1$. Since the two grids have different y-samplings (different grid points), the profiles were interpolated to a uniform grid of $N = 500$ points prior to comparison.

As shown in Fig. 6, L_2 decreases consistently between consecutive refinement pairs at every downstream station. Transitioning from level 7 to 8, L_2 ranges from 0.076 in the near wake (X/D = 2) to 0.021 at (X/D = 12). Transitioning from level 8 to 9, L_2 decreases to 0.033 and 0.007, respectively, at the same stations, confirming that the wake profile shape converges monotonically with refinement. Furthermore, the global domain-averaged velocity changes by less than 0.005% between levels 7 and 8 and less than 0.008% between levels 8 and 9, indicating negligible sensitivity of the bulk flow to further refinement beyond level 8. On the basis of these results, level 8 is selected for all production runs as an optimal approach that balances accuracy and computational resources.

In this study, an initial resolution of 2^8 (equivalent to 256 × 256 grid points) was selected to accurately construct the turbine geometry within the simulation domain. The turbine undergoes rotational motion, and its geometry is reconstructed at every time step. To control refinement, a custom wavelet-based algorithm was implemented (van Hooft et al., 2018), using thresholds based on both the velocity field and the volume fraction (turbine geometry). The mesh refines if the change in the velocity exceeds a 0.001 tolerance threshold; otherwise, the refinement level remains minimal (coarse mesh) within the undisturbed velocity region. At a high resolution of 2^8, each dimension has 256 cells, and the total number of cells in the domain is $2^8 \times 2^8$, which is equal to 65,536 cells. The turbine geometry is embedded within the dense cells at time step zero. The mesh adaptivity during the simulation is shown in Fig. 7. After the first step, the number of cells decreased from 65,536 to 6838 (the mesh was refined only around the turbine geometry). As the simulation evolved, the number of cells increased to approximately 20, 000 cells, which is approximately 30% of the initial cell number, following the evolution of the wake. The AMR strategy plays a critical role in achieving computational efficiency. Previous studies have shown that it can reduce the simulation time by more than 85% compared with simulations using uniform Cartesian grids (Aljber et al., 2024b; Lee et al., 2015; Popinet, 2020).

4.4. Model setup and BSM construction

To ensure consistency in the results comparison, the simulation setup closely followed the physical experiments (Olczak et al., 2016; Stallard et al., 2013a). For the single-row configuration with three turbines (D = 0.27 m, and Göttingen 804 blade profile), the computational domain was set to 21 × 14 m. The turbines were positioned at $X/D = 7$, leaving $X/D = 14$ of downstream length, and centered laterally with $Y/D = 7$ clearance on each side. For the remaining experiments, the domain was extended to 24 × 20 m. These dimensions were chosen to minimise the boundary effect on flow development.

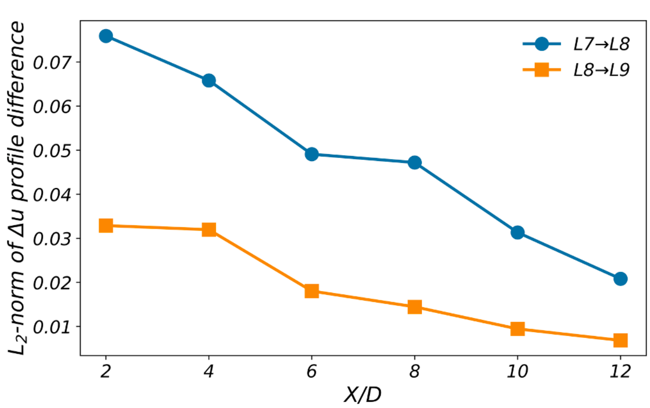

Fig. 6. L_2 norm of the streamwise velocity deficit profile difference between consecutive AMR maximum refinements (2^7, 2^8, 2^9) at X/D = 2, 4, 6, 8, 10, and 12.

Since the NS equations are elliptic in form, the flow field is computed simultaneously across the domain. This removes the need for a spin-up time but increases the sensitivity to boundary conditions. A CFL of 0.5 was used, with an inlet velocity of $u_0 = 0.47\ m/s$. The time step was automatically adjusted on the basis of the spatial resolution of the AMR with respect to the CFL condition. The velocity was imposed with Dirichlet boundary conditions at the inlet (left) and an outflow at the outlet (right) with Neumann conditions. The pressure at the inlet was set with Neumann conditions to maintain numerical stability. No-slip conditions were imposed on all the embedded boundaries. The dynamic viscosity was set to 0.01 (cell-face value), and the density was fixed at 1025 kg/m^3. A velocity damping coefficient of 0.065 was used for the single-row case, and 0.085 was used for the multirow configurations. These values were selected on the basis of multiple trial simulations and depend on the blockage effect, which is the proportion of the domain cross-section occupied by turbines. A greater blockage effect leads to a greater velocity reduction across the domain.

The BSM implementation followed the following three stages:

(I) Identify the blade geometry using the National Advisory Committee for Aeronautics (NACA) profile construction with Eq. (13):

$$naca00xx(x,y,a) = y^2 - \left(5\ \times a \times\ 0.2969\ \times \sqrt{x}\right)^2 - 0.126\ \times x - 0.3516\ \times x^2 + 0.2843\ \times x^3 - 0.1036\ \times x^4 \tag{13}$$

By using Eq. (13), any NACA profile can be constructed with a C routine function after the main parameters, such as the chord length, chamber thickness and position, are identified.

(II) Construct the turbines as a static geometry via the level-set function using Algorithm 1.

(III) impose time-dependent rotation on the turbines. For the turbine rotation in the BSM, Algorithm 2 was identified with the same information as Algorithm 1, and only the blade angle was modified to include an additional value updated at each time step. According to Ouro et al. (2019) and Stallard et al. (2013a), the rotational speed (omega) of the turbines was $\omega = 15.33\ rad/sec$. In the BSM, the turbine rotation is governed by $\theta(t) = \omega{\cdot}t$ and updated at each time step in Algorithm 2 as $\theta_b(t) = \theta_0^b + \theta(t)$.

Notably, when rotational motion was introduced, the simulation failed after the first time step was completed. This issue arose because the volume fraction field (representing the turbine) was defined at the initial condition, where the velocity was zero. Once the turbine begins rotating, the location of zero velocity shifts, leading to numerical instability and a simulation crash. To resolve this, an additional event was implemented to enforce zero velocity at all volume fraction locations throughout the simulation. The simulations were performed on a high-performance computing (HPC) cluster consisting of six nodes (with AMD EPYC 7352 CPUs with 24 cores). One node with 2 CPUs and 48 cores was used to conduct the simulation. Parallel computing was employed via OpenMPI, and a 100 s simulation was completed at approximately 4 to 8 min of wall-clock time. The velocity evolution stabilised after the first 40 s, and the velocity statistics were collected after 80 s.

4.5. Statistical metrices

To provide a better understanding of the validity of the NS-BSM approach, statistical measurements were calculated against the physical experiment using the root mean square error (RMSE) and the bias (B), and the accuracy was compared with the RANS-BEM results from Olczak et al. (2016).

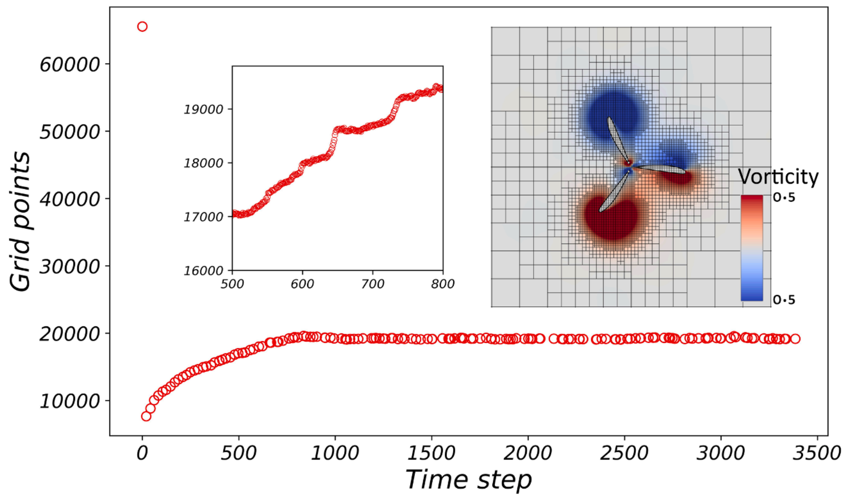

Fig. 7. The grid resolution adaptivity according to the number of cells (grid points) and the simulation time steps along with the initial adaptivity around the turbine blades.

Algorithm 1
Turbine geometry construction using a level-set formulation.

① *Specify the turbine array* (n_i, n_j)
② *Initialise the vertex-based level-set field* $\phi(\boldsymbol{x})$
③ *For each grid vertex* $\boldsymbol{x}_k$:
- For each turbine index (i, j):
  - *For each blade* $b \in \{1, 2, 3\}$:
    Define turbine centre $\boldsymbol{x}_d^{i,j}$
    - ■ *Define the effective blade angle*
      $\theta_b(t) = \theta_0^b$
    - ■ *Compute the rotated coordinates*
      $\boldsymbol{x}_r = \boldsymbol{R}_b(\theta_b)\left(\boldsymbol{x}_k - \boldsymbol{x}_d^{i,j}\right)$
    - ■ *Update the level-set value*
      $\phi(\boldsymbol{x}_k) = min\,(\phi(\boldsymbol{x}_k), \phi_b(\boldsymbol{x}_r))$

④ *Convert* ϕ *to volume fractions* c_s *and face fractions* f_s
⑤ *Apply geometry cleaning and boundary enforcement*

Algorithm 2
Time-dependent turbine geometry rotation.

① *Specify the turbine array* (n_i, n_j)
② *Initialise the vertex-based level-set field*$\phi(\boldsymbol{x})$
③ *For each grid vertex* $\boldsymbol{x}_k$:
- *For each turbine index* (i, j):
  - *For each blade* $b \in \{1, 2, 3\}$:
    - ■ *Define turbine centre:*$\boldsymbol{x}_d^{i,j}$
    - ■ *Compute the instantaneous angular position:*$\theta(t) = \omega{\cdot}t$
    - ■ *Define the effective blade angle*
      $\theta_b(t) = \theta_0^b + \theta(t)$
    - ■ *Compute the rotated coordinates*
      $\boldsymbol{x}_r = \boldsymbol{R}_b(\theta_b)\left(\boldsymbol{x}_k - \boldsymbol{x}_d^{i,j}\right)$
    - ■ *Update the level-set value*
      $\phi(\boldsymbol{x}_k) = min\,(\phi(\boldsymbol{x}_k), \phi_b(\boldsymbol{x}_r))$

④ *Convert* ϕ *to volume fractions* c_s *and face fractions*f_s
⑤ *Apply geometry cleaning and boundary enforcement*

$$RMSE = \sqrt{\frac{1}{n}\sum_{i=1}^{n}(m_i - o_i)^2} \tag{14}$$

$$B = \frac{1}{n}\sum_{i=1}^{n}(m_i - o_i) \tag{15}$$

where n is the number of samples, m_i is the modelled result, and o_i is the observed value.

5. Results

5.1. Single row

5.1.1. Three turbines

The simulation results of one row with three turbines (Stallard et al., 2013b) are shown in Fig. 8. The normalised velocities and turbulence intensity (TI) are presented in Fig. 8a and b. The normalised velocity is calculated as $\Delta u = 1 - u/u_0$, and the TI is calculated following Eq. (1).

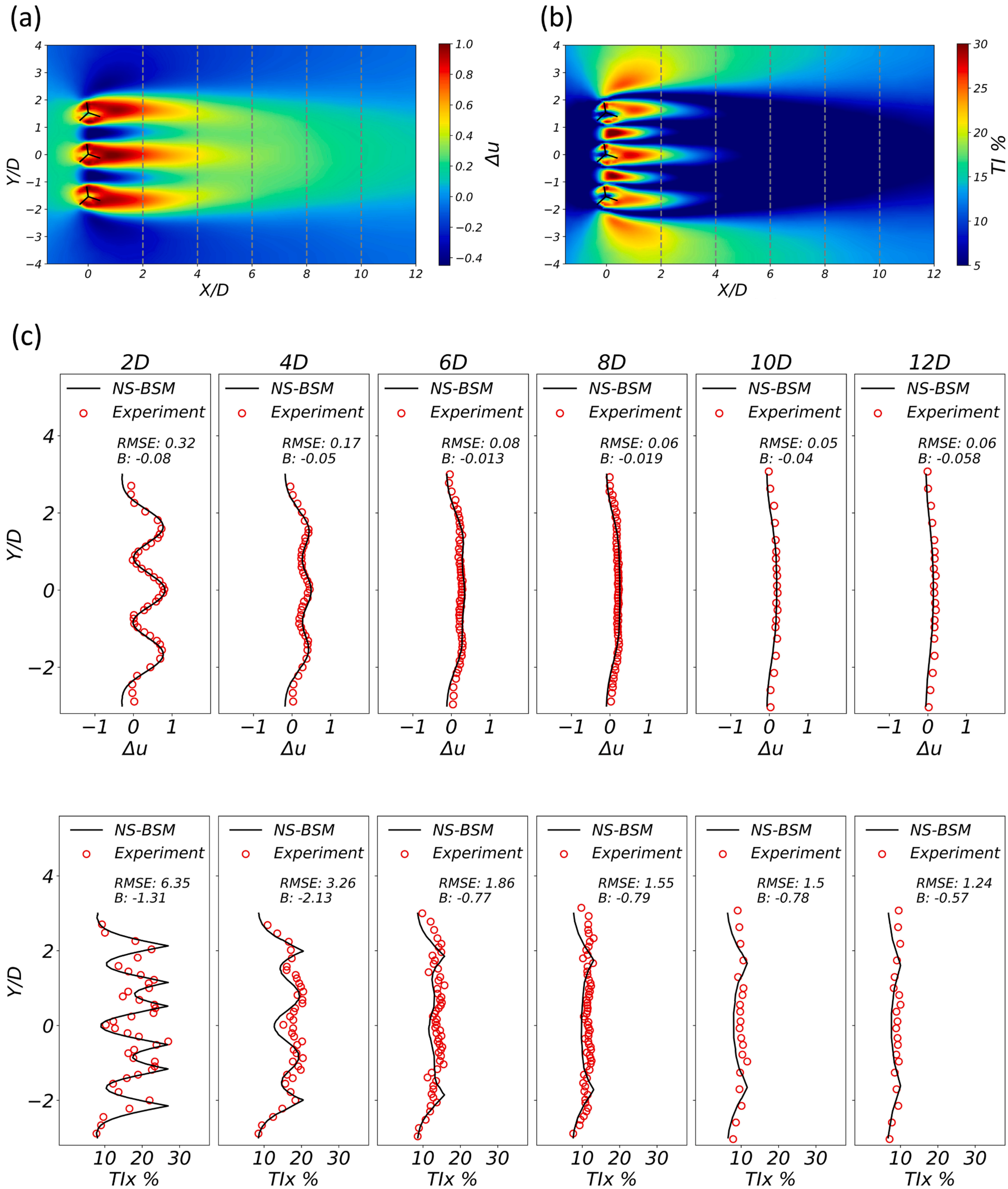

Fig. 8. The simulation results for the three turbines: (**a**) the normalised crosswise velocity at 80 s; (**b**) the turbulence intensity (TI) at 80 s; (**c**) cross comparison of the velocity (top) and TI (bottom) with the experimental results at 2D, 4D, 6D, 8D, 10D, and 12D downstream.

The individual wake evolution continues until approximately 6D is reached; then, it merges into a single wake. As shown in Fig. 8(c), the NS-BEM accurately captured the velocity variation downstream. At 2D, the RMSE and B were slightly greater, but the values improved downstream, reaching 0.06 and −0.058 for the RMSE and B, respectively, at 12D The crosswise velocities at the positions of the turbines were accurately captured by the NS-BSM, emphasising a reliable approach with a negligible computational cost. The TI was calculated at the same location as the normalised velocity. Although the RMSE and B were greater than those of the velocity comparison, the NS-BSM captured the TI variation across the farm. Like the velocity, the TI accuracy increased downstream, reaching 1.24 and −0.57 for the RMSE and B, respectively, at 12D In the high-turbulence zone downstream, at 2D and 4D, the NS-BSM overestimated the TI values by approximately 3% to 5%, and these values were minimised to less than 1% after 6D After 8D, the TI became approximately equal to the ambient turbulence because of mixing with the lateral flow. The NS-BSM method produced the main features of velocity deficit and TI downstream despite the fluctuating RMSE and B values. The BSM relies on the accurate and direct construction of the blade section geometry, and as discussed in Section 2, the downstream wake is generated because of the flow−blade section interaction. Therefore, even though the BSM is a reduced two-dimensional model, it produces flow-interaction physics with decent accuracy.

5.1.2. Five turbines

For the second case, five inline turbines in one row were simulated, as illustrated in Fig. 9. The results of the NS-BSM were compared with the experimental and RANS-BEM results from Olczak et al. (2016). The rotation of the turbines accelerated the velocity passing within the farm, as shown in Fig. 9a. At position 4D, the RANS-BEM overestimates the velocity passing between turbines by approximately $\Delta u = 10$ %. The NS-BSM presented a consistent velocity solution across the farm, albeit with slight underestimation of the velocity passing between turbines. The statistical metrics were approximately improved in the NS-BSM, with a RMSE of 0.05 and B of 0.017, compared with 0.066 and 0.03, respectively, in the RANS-BEM. Although the RANS-BEM represents a three-dimensional model, the method relies on one-dimensional annular momentum theory and two-dimensional hydrofoil data to identify the blade element force. Additionally, the RANS-BEM approximates the effect of the instantaneous velocity and predicts only the mean wake downstream without resolving vortex shedding. At 8D downstream, individual turbines wakes clearly merge in the NS-BSM results (Fig. 9b), whereas the RANS–BEM still shows distinct wakes until 10D. In the near-wake region at 4D (Fig. 9a), the velocity decreased by approximately 40% within the individual wakes. By 8D, the shear layers at the individual wake edges expanded and interacted through enhanced mixing with the ambient flow, entraining the high-velocity fluid between turbines and smoothing the transversed velocity profile. The velocity recovered at this location by approximately 20% (green color). The rotating blade sheds strong vortices, which enhance the turbulent kinetic energy at the individual wake edges and accelerate the merging of the wake structure.

5.2. Multiple rows

The tidal farm was extended to multiple rows, which increased the complexity level of wake generation and meandering downstream. Following the original experiments of Olczak et al. (2016), three tidal farm cases were simulated: Case I contained two rows with X = 4D longitudinal distance, Case II contained two rows with X = 8D longitudinal distance, and Case III contained three rows with X = 4D longitudinal distance. The rotational speed for the first row was fixed at 15.33 rad/s, whereas for turbines downstream, the rotational speed was reduced because of the effect of the upstream row. For the second-row turbines in cases I and II, the rotational speeds from the physical experiments were adopted (Table 1). For reference, the relative positions of the turbines in the second row are denoted as TT 'top', TM 'top middle', BB 'bottom', and BM 'bottom middle'. For Case III, three rows with a 4D longitudinal distance, the rows consisted of three, four, and five turbines from upstream to downstream, respectively. The rotational speed for the first row was 15.33 rad/s, and this value differed for the downstream turbines (Olczak et al., 2016). The three-row configuration is the most complicated case for numerical models because of the overlapping wake of 12 turbines from three rows. Assigning an individual rotational speed to each turbine introduced numerical instabilities during the simulations, which in turn affected the overall results. The rotational speed was imposed as an incremental blade angle at each time step (see Section 4.4, algorithm 2). However, as the number of turbines increased, applying distinct speeds required additional nested loops. Combined with complex flow interactions, this led to simulation breakdowns. To address this, the rotational speeds of the turbines in the second and third rows were averaged and uniformly applied across all the turbines in the corresponding row. This compromise ensured stable numerical performance while still producing reliable results. The rotational speeds were 12.724 rad/s and 11.866 rad/s for the second and third rows, respectively (Table 1). For reference, the relative positions of the turbines in the third row are TT 'top', TM 'top middle', MM 'middle middle', BM 'bottom middle', and BB 'bottom'.

5.2.1. Case I: two rows, 4D spacing

The results for Case I are shown in Fig. 10; the first row contains three turbines, and the second row contains four turbines. At position 6D, compared with the RANS-BEM, the NS-BSM accurately captured the velocity deficit and variation across the farm. The velocity reduction peaks were mostly underestimated by the RANS-BEM. Farther downstream at 8D, the performance of both numerical models was significantly lower than that at the 6D position. This deterioration is caused by the wake overlapping from the two rows induced by different turbine rotation speeds. At 8D, the individual wakes remain identifiable at the two middle turbines, whereas the upper and lower turbines illustrate a reduced individual wake effect because of rapid turbulence mixing with the ambient flow. At the two middle turbines, the velocity reduction was approximately 40%. The velocity reduction in both the NS-BEM and the RANS-BEM was approximately 47% at the two middle turbines. However, the NS-BEM produced relatively correct physical behavior

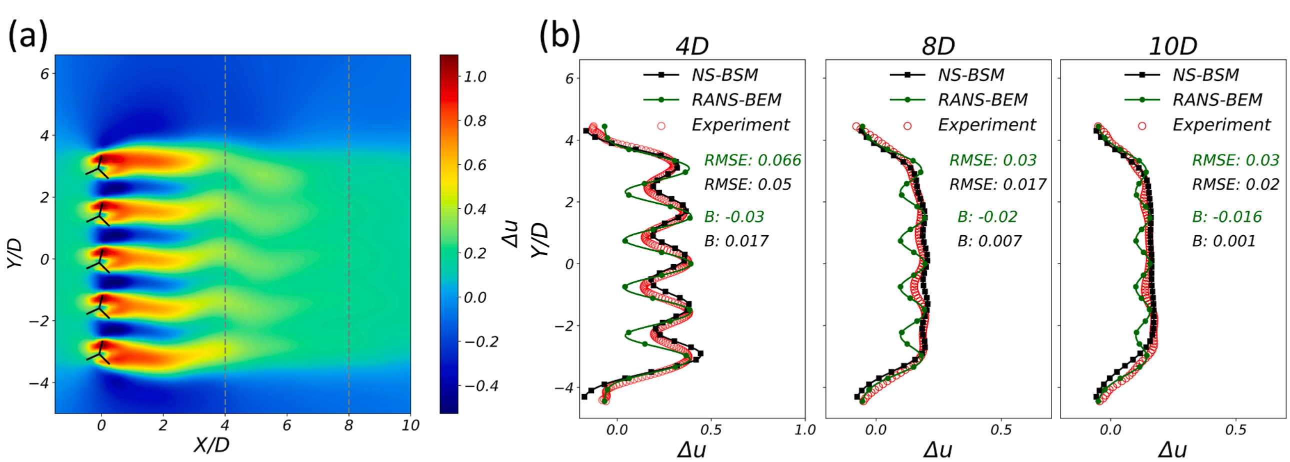

Fig. 9. Simulation results for the five turbines: (**a**) normalised crosswise velocity at 80 s and (**b**) cross comparison of the velocities of the RANS-BEM, NS-BSM, and flume experimental results at 4D, 8D, and 10D downstream.

Table 1
Rotational speed (ω) for the second and third rows of turbines downstream for three cases: Case I (X = 4D), Case II (X = 8D), and Case III (X = 4D). The locations of the turbines are presented in Figs. 10, 11, and 12. The turbines in the second row are TT 'top', TM 'top middle', BM 'bottom middle', and BB 'bottom', and those in the third row are TT 'top', TM 'top middle', MM 'middle middle', BM 'bottom middle', and BB 'bottom'.

Experiment	Second row				Third row				
	ω_{TT} (rad/s)	ω_{TM} (rad/s)	ω_{BM} (rad/s)	ω_{BB} (rad/s)	ω_{TT} (rad/s)	ω_{TM} (rad/s)	ω_{MM} (rad/s)	ω_{BM} (rad/s)	ω_{BB} (rad/s)
Case I (X = 4D)	13.49	11.95	11.8	13.64			✖		
Case II (X = 8D)	13.95	12.417	12.417	13.95			✖		
Case III (X = 4D)	12.724				11.866				

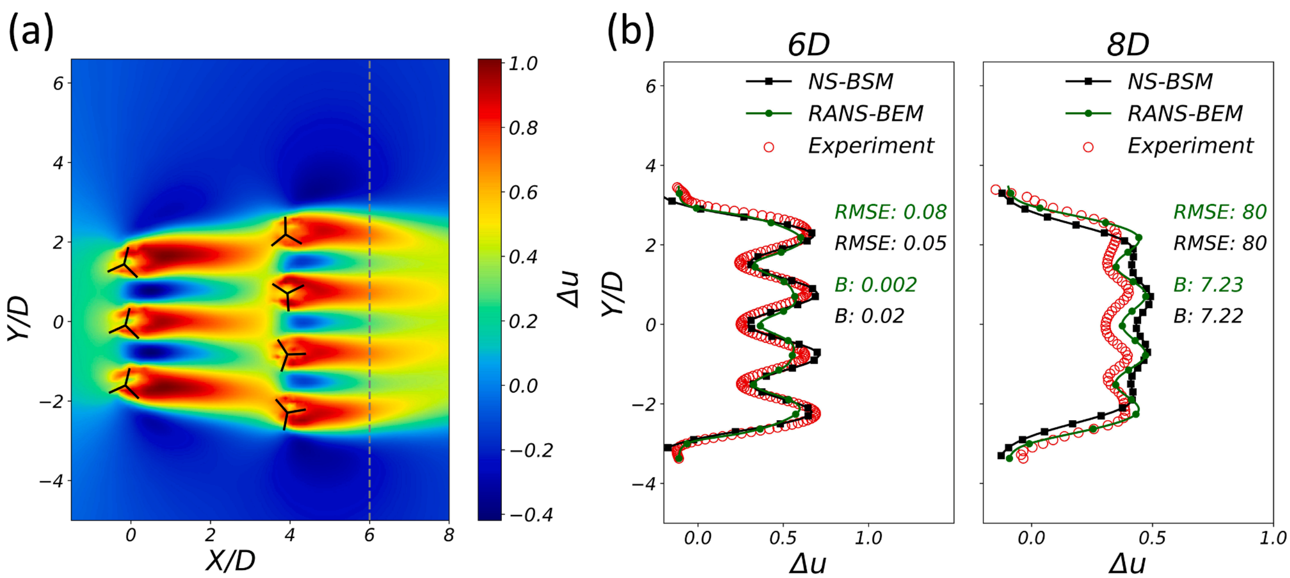

Fig. 10. Simulation results for Case I, the two rows of turbines with a longitudinal distance of X = 4D: (**a**) the normalised crosswise velocity at 100 s and (**b**) cross-comparison of the velocities of the RANS-BEM, NS-BSM, and experimental results at 6D and 8D downstream.

according to the experimental results. With respect to the RANS-BEM, the velocity deficit showed a uniform pattern across the farm without accounting for the relatively smoothened upper and lower wakes. Notably, the reduced velocity zone for the NS-BSM was narrower at 8D, which was caused by the elevated effect of the two rows given the shorter longitudinal distance. Turbines in the two-dimensional domain rotate with different rotational speeds, creating an area of reduced velocity downstream. The velocity at the lateral spaces near the farm (upper and lower) increases. Therefore, the coupling effect from the first and second rows accelerated turbulence mixing and velocity recovery

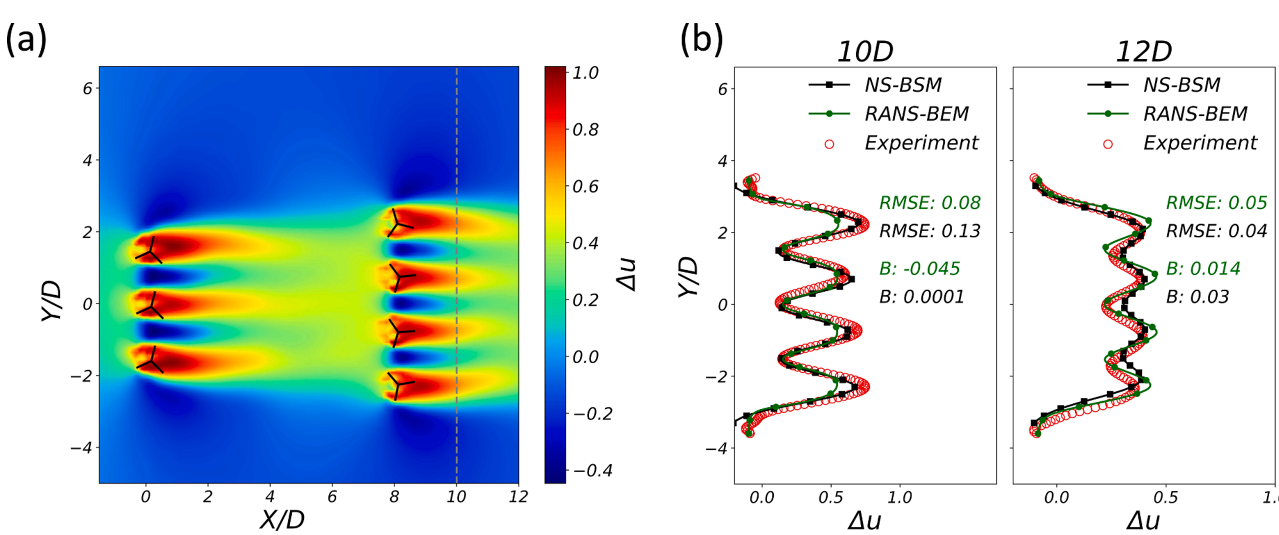

Fig. 11. Simulation results for Case II, the two rows of turbines with a longitudinal distance of X = 8D: (**a**) the normalised crosswise velocity at the second 100 s and (**b**) cross-comparison of the velocities of the RANS-BEM, NS-BSM, and experimental results at 10D and 12D downstream.

downstream. The two-dimensional setup amplifies this behavior since there is no vertical mixing.

5.2.2. Case II: two rows, 8D spacing

For Case II in Fig. 11, the longitudinal space between the two rows was extended to 8D, which allowed for a higher rotational speed than that in Case I (Table 1). At 10D, the velocity reduction in the individual wake was approximately 75%, whereas in the RANS-BEM, the velocity reduction was approximately 55%. The RMSE was 0.13 greater for the NS-BSM than for the RANS-BEM (0.08). However, the B improved to 0.0001 for the NS-BSM compared with −0.045 for the RANS-BEM. Compared with that in Case I (Fig. 10), the velocity at the lateral edge of the farm, at 12D, was improved. This improvement is due to the greater distance between the two rows. For Case I, the close longitudinal distance between the two rows increased turbulence mixing, and the confined conditions of the two-dimensional domain with no vertical mixing caused a squeezing region downstream. In Case II, this effect was reduced by the recovery distance before the second row. The NS-BSM slightly underestimates the velocity between turbines at 12D by approximately 5% relative to the experimental measurements, whereas the RANS-BEM overestimates velocities both within the individual wakes and in the interturbine regions. In Case II, the individual wakes of the upper and lower turbines remain distinguishable at 12D, reflecting the longer recovery distance between the two rows. In contrast, in Case I, the second row is exposed to higher ambient turbulence, which accelerates wake mixing and results in smoother, less distinct wakes for the upper and lower turbines.

5.2.3. Case III: three rows, 4D spacing

The results of the NS-BSM are compared with those of the RANS-BEM and the physical experiment for Case III in Fig. 12. At position 10D, the velocity experienced a major reduction, approximately 75%, at the upper and lower turbines of the farm, whereas the velocity reduction was relatively consistent for the middle turbines, approximately 55%. The staggered arrangement of the turbines in three rows enhanced the velocity divergence toward the upper and lower edges of the farm. At the upper and lower turbines, the higher velocity increased the thrust force (Olczak et al., 2016), creating uneven velocity deficit across the farm. The NS-BSM accurately captured this variation in velocity at 10D because of the accurate construction of the rotors. In the RANS-BEM, the fluctuations were consistent, and the two velocity reduction peaks at the two edges were not captured. As shown in Fig. 12(a), the largest velocity reduction, approximately 80%, occurred between the first and second rows at 2D The turbines in the middle received higher velocities because of the blockage effect induced by the rotation of the turbines at the edges. The velocity reduction between the second and third rows was approximately 70% at 6D. This velocity reduction pattern illustrated the benefits of a staggered array arrangement in which the velocity recovery increased, allowing a higher velocity for the turbines downstream.

5.3. Farm boundary and wake interaction

The downstream vorticity expansion (top) for Cases I, II, and III, alongside the velocity vectors (bottom) for the same layouts with multiple rows, are shown in Fig. 13. In all the cases, the strongest vorticity appears at the lateral edge of the farm (Fig. 13, top), where the turbine wakes directly interact with the surrounding high-velocity flow. This behavior stems from velocity divergence induced by the rotating turbines, which is further intensified at the edges where turbines operate at higher rotational speeds than those in the middle. The elevated vorticity persists for approximately 4D downstream of the last row in all the cases. The short spacing between the first and second rows in Cases I and III enhances the wake–wake interactions, accelerating the flow at the lateral boundaries. As shown in Fig. 13(a) and (c), the velocity vectors are deflected inwards toward the wake zone, which causes the lateral boundary to contract (see also Figs. 10(b) and 12(b)). Case II exhibits weaker contraction because of the longer recovery distance between rows.

This lateral boundary contraction was not observed by the RANS-BEM results of (Olczak et al., 2016) (Figs. 8–12) or by the LES-ALM of Ouro et al. (2019), likely because the three-dimensional wake parameterisation smoothed out the two-dimensional mixing effects. The NS-BSM approach successfully resolves the velocity deficits while maintaining substantially lower computational costs. Despite its inherent two-dimensional limitations, the NS-BSM provides a practical and efficient tool for array design, which is particularly valuable as the TSE sector moves from pilot-scale to commercial-scale deployment.

6. Discussion

Three-dimensional RANS models can offer reasonable estimates of the mean wake deficit (Apsley et al., 2018; Olczak et al., 2016). However, RANS models do not resolve instantaneous wake dynamics. Three-dimensional LES can capture instantaneous wake dynamics and time-dependent structural loading but with high computational demand. (Ouro et al., 2019) reproduced the physical experiments of

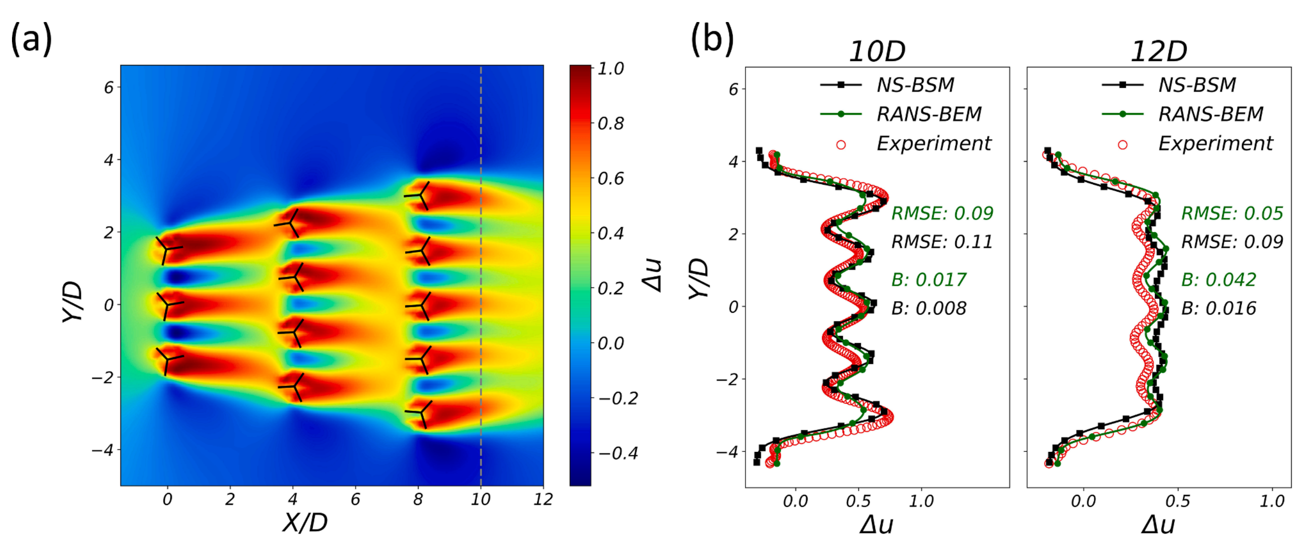

Fig. 12. Simulation results for Case III (three rows of turbines with longitudinal distances of X = 4D): (**a**) the normalised crosswise velocity during the second 100 s and (**b**) cross comparison of the velocities of the RANS-BEM, NS-BSM, and experimental results at 10D and 12D downstream.

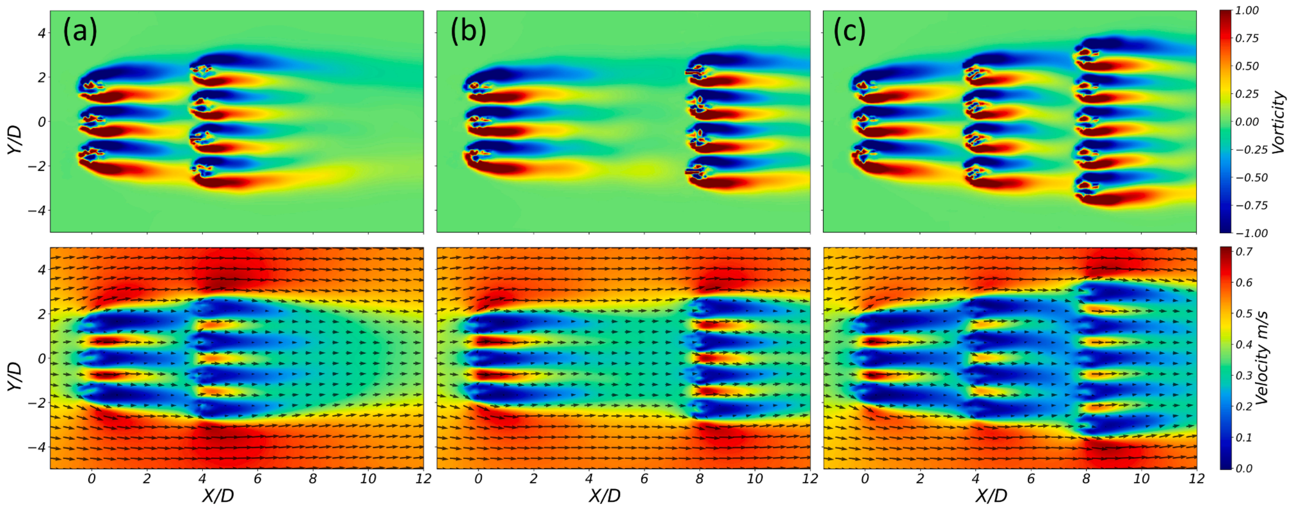

Fig. 13. Vorticity expansion downstream along with the velocity vectors for Cases I, II, and III with multiple rows of turbines in a staggered layout: (a) Case I, two rows with X/D equal to 4 longitudinal distances; (b) Case II, two rows with X/D equal to 8 longitudinal distances; (c) Case III, three rows with X/D equal to 4 longitudinal distances.

(Olczak et al., 2016; Stallard et al., 2013a) using a three-dimensional LES model where the turbines were presented via the ALM. The authors reported that they conducted simulations for 360 s on a supercomputer using 51 processors, and the simulation time was 15 days. The LES-ALM accounted for high resolution (0.01 m and 0.005 m at the turbines and wake region, respectively) to capture the velocity and TI fluctuations in a single row of three turbines. However, with respect to the two rows, the model did not produce an accurate velocity deficit in the near-wake region at 6D in Case I (two rows with X = 4D longitudinal distance) or at 10D in Case II (two rows with X = 8D longitudinal distance). One reason could be that the ALM method presents the turbine via drag forces within the mesh nodes, which does not present an accurate blade geometry. (Kang et al., 2014) reported that simplified representative models that neglect turbine geometry cannot capture key instability mechanisms responsible for the wake meandering observed in experiments. Wake structures such as tip vortices generally lose coherence a few diameters downstream, whereas large-scale wake meandering can persist much further. Therefore, not only velocity deficit recovery but also the spatial and temporal characteristics of turbulent structures must be considered.

All the cases in this study were simulated for 100 s since the velocity regime stabilised after 40 s. The simulation took approximately 4 to 8 min of wall-clock time. The AMR levels were defined between 2^5 (coarse) and 2^8 (fine), corresponding to spatial resolutions of approximately 0.75 m for the ambient flow and 0.09 m in the turbines and wake regions. Comparatively, the high resolution in the RANS-BEM from (Olczak et al., 2016) around the turbines and in the wake region was approximately 0.05 m in the X direction and approximately 0.03 m in the Y and Z directions.

The NS scheme in Basilisk essentially supports direct numerical simulation (DNS) since it does not include an inherent turbulence model or subgrid-scale parameterisation. However, to implement a DNS, the model must solve all physical scales (Kolmogorov and near-wall scales) in space and time (Moin and Mahesh, 1998). Hence, the grid spacing Δ must be sufficiently small relative to the Kolmogorov (dissipation) length scale η and satisfy the condition $\Delta/\eta \lesssim 1$, where η is calculated as follows:

$$\eta = \left(\frac{\nu^3}{\varepsilon}\right)^{1/4} \tag{16}$$

where ν is the kinematic viscosity (in this study, $\nu = \frac{\mu}{\rho} \approx 9.75 \times 10^{-6} m^2/s$) and ε is the kinetic energy dissipation rate (m^2/s^3), which represents the kinetic energy loss at small turbulent scales. ε is calculated as follows:

$$\varepsilon = 2\nu D_{ij} D_{ij} \tag{17}$$

where D_{ij} is the deformation tensor from Eq. (2).

Using Eqs. (16) and (17), a statistical analysis was conducted for the spatial resolution in Case I (two rows with X = 4D longitudinal distance). The proportion Δ/η was found to be between approximately 0.07 and 693, with an average value of 40.8, which means that on average, the grid cells are approximately 40.8 times greater than 1. This indicated that the NS-BSM does not satisfy a DNS condition. The Δ/η average of 40.8, however, suggested a weighted proportion toward the DNS value of 1. To investigate this proportion further, a probability density function (PDF) test was conducted, as presented in Fig. 14(a). The PDF for a randomly selected computational cell represents the probability that the resolution proportion Δ/η falls within a given interval (0.07 and 693). The proportion Δ/η is depicted on a logarithmic scale in Fig. 14 for ease of illustration, with two reference lines of $\Delta/\eta = 1$ and 10 and an average value of 40.8. The majority of the Δ/η values range between 1 and 100, with approximately 80% of the proportion being less than 40.8, mostly in the turbines and wake region where the high resolution is concentrated, as presented in Fig. 14(b).

Although the NS-BSM simulation with a maximum AMR level of 2^8 ($\Delta \approx 0.09$ m) did not satisfy the DNS resolution requirements, the computational effort was strategically concentrated in regions governing the turbine–flow interaction and wake evolution (Fig. 14(b)). High accuracy was achieved by using the EBC, ensuring an accurate geometric representation of the turbines. Additionally, the two-dimensional simulation reduced the computational demand while maintaining high performance.

Therefore, the numerical tests and validations presented in this study emphasise the applicability of the hypothesis that the turbine can be accurately presented and simulated on the basis of the blade cross section.

7. Conclusion

Quantifying flow dynamics is a critical step toward optimising tidal array design. While three-dimensional models provide valuable insights into wake behavior, flow recovery, and turbine interaction, their high computational cost continues to be a major barrier to large-scale applications. The proposed two-dimensional NS-BSM approach integrates

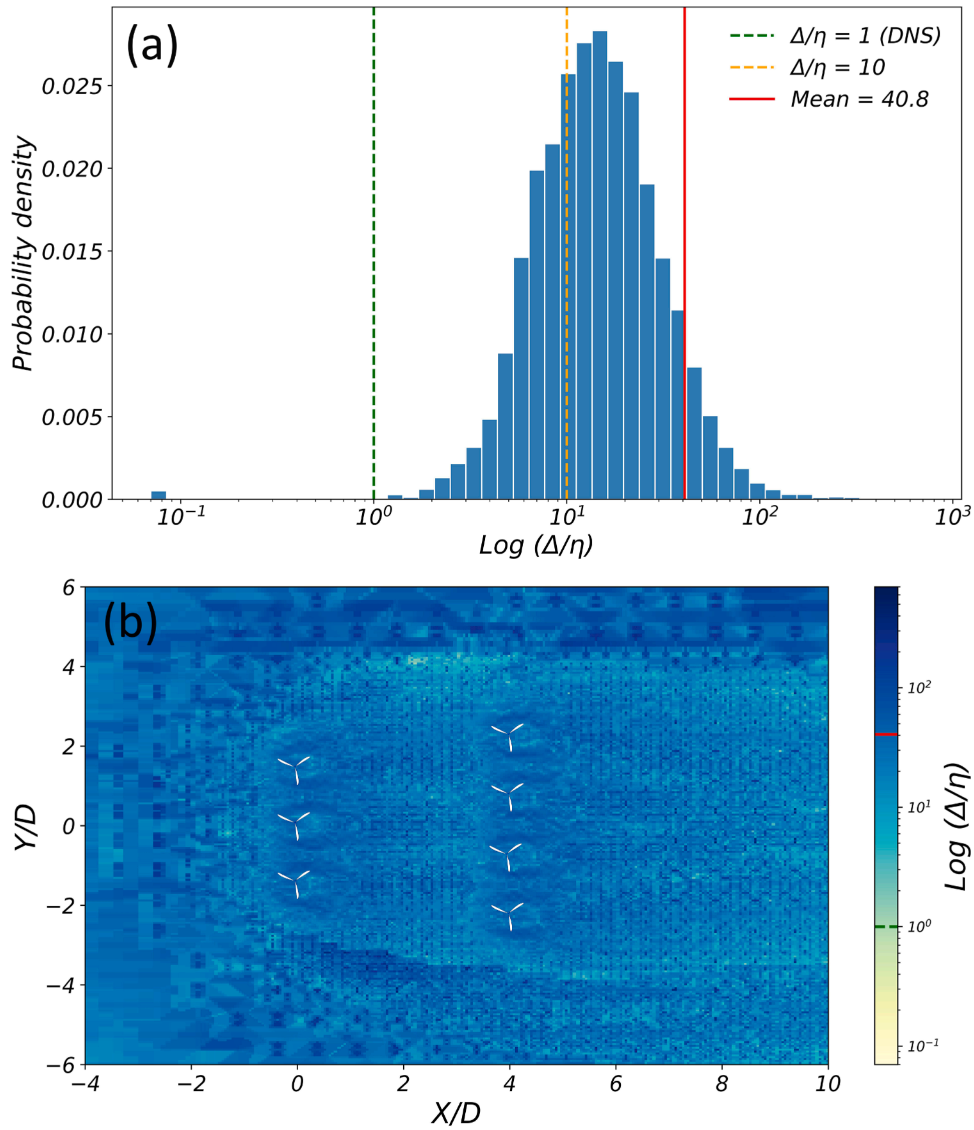

Fig. 14. (**a**) Probability density histogram of the proportion Δ/η values across a randomly selected computational cell, with vertical reference lines at $\Delta/\eta = 1$ and 10 and an average of 40.8. (**b**) Spatial distribution of the proportion Δ/η values within the computational domain.

a simplified yet effective turbine representation with an AMR-based solver. This approach demonstrates that two-dimensional simulations can serve as a practical compromise between physical realism and computational efficiency. The studied cases consumed approximately 6 min on average of wall-clock time to simulate 100 s of turbine-flow interaction. The NS-BSM method was shown to reproduce key flow features, including wake expansion, velocity deficit and recovery distance, in good agreement with experimental and numerical references.

The NS-BSM offers a valuable engineering tool for rapid scenario testing and early-stage optimisation of turbine layouts where multiple array configurations must be evaluated. However, its primary limitation lies in the two-dimensional framework, which cannot resolve vertical flow structures. This restricts its applicability to processes such as wave–current interactions, vertical mixing, sediment transport, and seabed scouring. Similarly, the simplified rotor representation limits its ability to predict detailed hydrodynamic loads on turbine components and support structures. Consequently, the NS-BSM cannot serve as a replacement for three-dimensional CFD models where such processes are of primary interest.

Despite these limitations, the NS-BSM fills an important niche in the tidal array modelling hierarchy. It provides a computationally efficient alternative for array-scale layout optimisation, bridging the gap between overly simplified analytical models and computationally demanding three-dimensional simulations. The horizontal wake dynamics captured by the NS-BSM are sufficient to estimate array-scale power extraction using actuator disc theory, offering a practical pathway to performance assessment without full three-dimensional resolution. Furthermore, the computed array-scale velocity fields can serve as boundary conditions for localised three-dimensional simulations, enabling detailed rotor-level analysis at reduced computational cost. Future work will focus on two directions: coupling the NS-BSM with reduced-order models to incorporate vertical flow processes and integrating adaptive levelised cost of energy (LCOE) calculations to extend the framework toward economic tidal farm optimisation.

Acknowledgements

The first author would like to thank the Hiroshima University SPRING Research Fellowship for supporting this study. This study is supported by the JSPS Grant-in-Aid for Scientific Research (B) (Grant No. 24 K00991). This work was also supported by JST Grant Number, JPMJPF2404.

CRediT authorship contribution statement

Morhaf Aljber: Writing – original draft, Visualization, Validation, Software, Resources, Methodology, Investigation, Formal analysis, Conceptualization. **Han Soo Lee:** Writing – review & editing, Visualization, Validation, Supervision, Resources, Project administration, Methodology, Investigation, Funding acquisition, Formal analysis, Conceptualization.

Declaration of competing interest

The authors declare that they have no known competing financial interests or personal relationships that could have appeared to influence the work reported in this paper.

References

Ahmed, U., Apsley, D.D., Afgan, I., Stallard, T., Stansby, P.K., 2017. Fluctuating loads on a tidal turbine due to velocity shear and turbulence: comparison of CFD with field data. Renew. Energy 112, 235–246. https://doi.org/10.1016/j.renene.2017.05.048.
Aljber, M., Jeong, J.S., Cabrera, J.S., Calvo, M.A.S., Chisale, S.W., Williams, Z., Lee, H.S., 2024a. Optimal site selection and potential power assessment for tidal power generation in the Seto Inland Sea, Japan, based on high-resolution ocean modelling and multicriteria analysis. Appl. Energy 372, 123843. https://doi.org/10.1016/J.APENERGY.2024.123843.
Aljber, M., Lee, H.S., Jeong, J.S., 2025. Integrated tidal power potential in the Seto Inland Sea in Japan with cost–benefit analysis. Appl. Energy 395, 126205. https://doi.org/10.1016/J.APENERGY.2025.126205.
Aljber, M., Lee, H.S., Jeong, J.S., Cabrera, J.S., 2024b. Tsunami inundation modelling in a built-In coastal environment with adaptive mesh refinement: the Onagawa benchmark test. J. Mar. Sci. Eng. 12, 177. https://doi.org/10.3390/jmse12010177.
Aljber, M., Sakanoue, G., Jeong, J.-S., Cabrera, J.S., Lee, H.S., 2023. Assessment of potential tidal power sites in the Seto Inland Sea, Japan using multi-criteria evaluation. In: Caetano, N.S., Felgueiras, M.C. (Eds.), Proceedings of the 9th International Conference on Energy and Environment Research. Springer Nature Switzerland, Cham, pp. 281–289.
Apsley, D.D., Stallard, T., Stansby, P.K., 2018. Actuator-line CFD modelling of tidal-stream turbines in arrays. J. Ocean Eng. Mar. Energy 4, 259–271. https://doi.org/10.1007/s40722-018-0120-3.
Arup, O., 2016. Department of energy and climate change review of renewable electricity generation cost and technical assumptions study report job number job number review of renewable electricity generation cost and technical assumptions study report report ref | final |.
Baba-Ahmadi, M.H., Dong, P., 2017. Validation of the actuator line method for simulating flow through a horizontal axis tidal stream turbine by comparison with measurements. Renew. Energy 113, 420–427. https://doi.org/10.1016/j.renene.2017.05.060.
Bae, Y.H., Kim, K.O., Choi, B.H., 2010. Lake Sihwa tidal power plant project. Ocean Eng. 37, 454–463. https://doi.org/10.1016/j.oceaneng.2010.01.015.
Basilisk, 2025. Basilisk flow Solver [WWW Document]. URL. https://basilisk.fr/. accessed 12.11.25.
Bell, J.B., Colella, P., Glaz, H.M., 1989. A second-order projection method for the incompressible navier-stokes equations. J. Comput. Phys. 85, 257–283. https://doi.org/10.1016/0021-9991(89)90151-4.
Cheynet, E., Li, L., Jiang, Z., 2024. Metocean conditions at two Norwegian sites for development of offshore wind farms. Renew. Energy 224, 120184. https://doi.org/10.1016/J.RENENE.2024.120184.
Claire Cohen, Tim Baker, 2020. Lessons learnt from MeyGen Phase 1A final summary report.
Díaz, H., Guedes Soares, C., 2020. Review of the current status, technology and future trends of offshore wind farms. Ocean Eng. 209, 107381. https://doi.org/10.1016/J.OCEANENG.2020.107381.
Divett, T., Vennell, R., Stevens, C., 2013. Optimization of multiple turbine arrays in a channel with tidally reversing flow by numerical modelling with adaptive mesh. Philos. Trans. A. Math. Phys. Eng. Sci. 371. https://doi.org/10.1098/rsta.2012.0251.
Divett, T., Vennell, R., Stevens, C., 2016. Channel-scale optimisation and tuning of large tidal turbine arrays using LES with adaptive mesh. Renew. Energy 86, 1394–1405. https://doi.org/10.1016/j.renene.2015.09.048.
European Marine Energy Centre Ltd., 2009. Assessment of Tidal Energy Resource. Tech. Rep. EMEC.
Garcia-Novo, P., Inubuse, M., Matsuno, T., Kyozuka, Y., Archer, P., Matsuo, H., Henzan, K., Sakaguchi, D., 2024. Characterization of the wake generated downstream of a MW-scale tidal turbine in Naru Strait, Japan, based on vessel-mounted ADCP data. Energy 299, 131453. https://doi.org/10.1016/j.energy.2024.131453.
Gaurier, B., Carlier, C., Germain, G., Pinon, G., Rivoalen, E., 2020. Three tidal turbines in interaction: an experimental study of turbulence intensity effects on wakes and turbine performance. Renew. Energy 148, 1150–1164. https://doi.org/10.1016/j.renene.2019.10.006.
Gauvin-Tremblay, O., Dumas, G., 2022. Hydrokinetic turbine array analysis and optimization integrating blockage effects and turbine-wake interactions. Renew. Energy 181, 851–869. https://doi.org/10.1016/j.renene.2021.09.003.
Ghigo, A.R., Popinet, S., Wachs, A., 2023. A conservative finite volume cut-cell method on an adaptive Cartesian tree grid for moving rigid bodies in incompressible flows.
Guerra, M., Hay, A.E., 2024. Field observations of the wake from a full-scale tidal turbine array. Renew. Energy 226, 120315. https://doi.org/10.1016/j.renene.2024.120315.
Hasselman, D.J., Hemery, L.G., Copping, A.E., Fulton, E.A., Fox, J., Gill, A.B., Polagye, B., 2023. Scaling up' our understanding of environmental effects of marine renewable energy development from single devices to large-scale commercial arrays. Sci. Total. Environ. 904, 166801. https://doi.org/10.1016/j.scitotenv.2023.166801.
Kang, S., Yang, X., Sotiropoulos, F., 2014. On the onset of wake meandering for an axial flow turbine in a turbulent open channel flow. J. Fluid Mech. 744, 376–403. https://doi.org/10.1017/jfm.2014.82.
Kyuden Mirai Ltd, 2025. Commencement of installation of Japan's first commercial-scale large-scale tidal current generator (Completed modification of tidal current generator and installed off the coast of Goto City, Nagasaki Prefecture).
Lagrée, P.Y., Staron, L., Popinet, S., 2011. The granular column collapse as a continuum: validity of a two-dimensional Navier-Stokes model with a Î(I)-rheology. J. Fluid Mech. 686, 378–408. https://doi.org/10.1017/jfm.2011.335.
Lee, H.S., Shimoyama, T., Popinet, S., 2015. Impacts of tides on tsunami propagation due to potential Nankai Trough earthquakes in the Seto Inland Sea, Japan. J. Geophys. Res. Oceans 120, 6865–6883. https://doi.org/10.1002/2015JC010995.
Li, M., Cao, S., Zhu, X., Xu, Y., 2022. Techno-economic analysis of the transition towards the large-scale hybrid wind-tidal supported coastal zero-energy communities. Appl. Energy 316, 119118. https://doi.org/10.1016/j.apenergy.2022.119118.
Lieber, L., Fraser, S., Coles, D., Nimmo-Smith, W.A.M., 2024. Sheared turbulent flows and wake dynamics of an idled floating tidal turbine. Nat. Commun. 15. https://doi.org/10.1038/s41467-024-52578-x.
Limare, A., Popinet, S., Josserand, C., Xue, Z., Ghigo, A., 2023. A hybrid level-set /embedded boundary method applied to solidification-melt problems. J. Comput. Phys. 474, 111829. https://doi.org/10.1016/j.jcp.2022.111829.
Liu, X., Ren, T., Cen, Y., Lu, J., Wang, X., Yu, F., Liu, H., Yuan, S., 2025. Impact of rotation speed and direction on adjacent tidal turbine hydrodynamics in close lateral spacings. Ocean Eng. 327, 120983. https://doi.org/10.1016/j.oceaneng.2025.120983.
Marsh, P., Penesis, I., Nader, J.R., Cossu, R., 2021a. Multi-criteria evaluation of potential Australian tidal energy sites. Renew. Energy 175, 453–469. https://doi.org/10.1016/j.renene.2021.04.093.
Marsh, P., Penesis, I., Nader, J.R., Cossu, R., Auguste, C., Osman, P., Couzi, C., 2021b. Tidal current resource assessment and study of turbine extraction effects in Banks Strait, Australia. Renew. Energy 180, 1451–1464. https://doi.org/10.1016/j.renene.2021.08.051.
Masters, I., Chapman, J.C., Willis, M.R., Orme, J.A.C., 2011. A robust blade element momentum theory model for tidal stream turbines including tip and hub loss corrections. J. Mar. Eng. Technol. 10, 25–35. https://doi.org/10.1080/20464177.2011.11020241.
McAdam, R.A., Houlsby, G.T., Oldfield, M.L.G., 2013. Experimental measurements of the hydrodynamic performance and structural loading of the transverse horizontal Axis water turbine: part 1. Renew. Energy 59, 105–114. https://doi.org/10.1016/j.renene.2013.03.016.
Mehta, D., van Zuijlen, A.H., Koren, B., Holierhoek, J.G., Bijl, H., 2014. Large Eddy simulation of wind farm aerodynamics: a review. J. Wind Eng. Ind. Aerodyn. 133, 1–17. https://doi.org/10.1016/j.jweia.2014.07.002.
Mohammadi, Y., GKnight, B., 2025. CFD calculations of a hydrokinetic turbine in uniform and sheared inflows. Ocean Eng. 335, 121548. https://doi.org/10.1016/j.oceaneng.2025.121548.
Moin, P., Mahesh, K., 1998. Direct numerical simulation: a tool in turbulence research. Annu. Rev. Fluid Mech. 30, 539–578.
Ning, S.A., Hayman, G., Damiani, R., Jonkman, J., 2015. Development and validation of a new blade element momentum skewed-wake model within AeroDyn.
Nuernberg, M., Tao, L., 2018. Three dimensional tidal turbine array simulations using OpenFOAM with dynamic mesh. Ocean Eng. 147, 629–646. https://doi.org/10.1016/j.oceaneng.2017.10.053.
Ocean energy Europe, 2025. Ocean energy stats and trends 2024.
Olczak, A., Stallard, T., Feng, T., Stansby, P.K., 2016. Comparison of a RANS blade element model for tidal turbine arrays with laboratory scale measurements of wake velocity and rotor thrust. J. Fluids Struct. 64, 87–106. https://doi.org/10.1016/j.jfluidstructs.2016.04.001.
Ouro, P., Harrold, M., Stoesser, T., Bromley, P., 2017. Hydrodynamic loadings on a horizontal axis tidal turbine prototype. J. Fluids Struct. 71, 78–95. https://doi.org/10.1016/j.jfluidstructs.2017.03.009.
Ouro, P., Mullings, H., Christou, A., Draycott, S., Stallard, T., 2024. Wake characteristics behind a tidal turbine with surface waves in turbulent flow analyzed with large-eddy simulation. Phys. Rev. Fluids 9. https://doi.org/10.1103/PhysRevFluids.9.034608.
Ouro, P., Nishino, T., 2021. Performance and wake characteristics of tidal turbines in an infinitely large array. J. Fluid Mech. 925. https://doi.org/10.1017/jfm.2021.692.
Ouro, P., Ramírez, L., Harrold, M., 2019. Analysis of array spacing on tidal stream turbine farm performance using large-eddy Simulation. J. Fluids Struct. 91, 102732. https://doi.org/10.1016/j.jfluidstructs.2019.102732.
Popinet, S., 2020. A vertically-lagrangian, non-hydrostatic, multilayer model for multiscale free-surface flows. J. Comput. Phys. 418, 109609. https://doi.org/10.1016/j.jcp.2020.109609.
Popinet, S., 2018. Numerical models of surface tension. Annu. Rev. Fluid Mech. 50, 49–75. https://doi.org/10.1146/annurev-fluid-122316-045034.
Popinet, S., 2011. Lecture notes introduction to numerical methods for interfacial flows.

Popinet, S., 2009. An accurate adaptive solver for surface-tension-driven interfacial flows. J. Comput. Phys. 228, 5838–5866. https://doi.org/10.1016/j.jcp.2009.04.042.

Popinet, S., 2003. Gerris: a tree-based adaptive solver for the incompressible Euler equations in complex geometries. J. Comput. Phys. 190, 572–600. https://doi.org/10.1016/S0021-9991(03)00298-5.

Posa, A., Viola, I.M., Broglia, R., 2024. Influence of the tip speed ratio on the wake dynamics and recovery of axial-flow turbines. Phys. Fluids 36. https://doi.org/10.1063/5.0203285.

Ramanan, C.J., Lim, K.H., Kurnia, J.C., Roy, S., Bora, B.J., Medhi, B.J., 2024. Towards sustainable power generation: recent advancements in floating photovoltaic technologies. Renew. Sustain. Energy Rev. 194, 114322. https://doi.org/10.1016/J.RSER.2024.114322.

Sabia, C., Radeke, L.M., Frigerio, G., Martinoli, L., Ulbricht, M., Schultz, H.J., Barbato, M.C., 2026. PIV validation of the CFD simulation of single-phase velocity field in spiral jet mills. Adv. Powder. Technol. 37, 105179. https://doi.org/10.1016/J.APT.2026.105179.

Smart, G., Noonan, M., 2018. Tidal stream and wave energy cost reduction and industrial benefit summary analysis.

Song, S., Demirel, Y.K., Atlar, M., Shi, W., 2020. Prediction of the fouling penalty on the tidal turbine performance and development of its mitigation measures. Appl. Energy 276, 115498. https://doi.org/10.1016/j.apenergy.2020.115498.

Sorensen, J.N., Mikkelsen, R.F., Henningson, D.S., Ivanell, S., Sarmast, S., Andersen, S.J., 2015. Simulation of wind turbine wakes using the actuator line technique. Philos. Trans. R. Soc. A: Math. Phys. Eng. Sci. 373, 20140071. https://doi.org/10.1098/rsta.2014.0071.

Stallard, T., Collings, R., Feng, T., Whelan, J., 2013a. Interactions between tidal turbine wakes: experimental study of a group of three-bladed rotors. Philos. Trans. R. Soc. A: Math. Phys. Eng. Sci. 371, 20120159. https://doi.org/10.1098/rsta.2012.0159.

Stallard, T., Collings, R., Feng, T., Whelan, J., 2013b. Interactions between tidal turbine wakes: experimental study of a group of three-bladed rotors. Philos. Trans. R. Soc. A: Math. Phys. Eng. Sci. 371, 20120159. https://doi.org/10.1098/rsta.2012.0159.

Stallard, T., Feng, T., Stansby, P.K., 2015. Experimental study of the mean wake of a tidal stream rotor in a shallow turbulent flow. J. Fluids Struct. 54, 235–246. https://doi.org/10.1016/j.jfluidstructs.2014.10.017.

van Hooft, J.A., Popinet, S., van Heerwaarden, C.C., van der Linden, S.J.A., de Roode, S.R., van de Wiel, B.J.H., 2018. Towards adaptive grids for atmospheric boundary-layer simulations. Bound. Layer Meteorol. 167, 421–443. https://doi.org/10.1007/s10546-018-0335-9.

Wallwork, J.G., Angeloudis, A., Barral, N., Mackie, L., Kramer, S.C., Piggott, M.D., 2024. Tidal turbine array modelling using goal-oriented mesh adaptation. J. Ocean Eng. Mar. Energy 10, 193–216. https://doi.org/10.1007/s40722-023-00307-9.

Wang, M., Avital, E.J., Bai, X., Ji, C., Xu, D., Williams, J.J.R., Munjiza, A., 2020. Fluid–structure interaction of flexible submerged vegetation stems and kinetic turbine blades. Comput. Part Mech. 7, 839–848. https://doi.org/10.1007/s40571-019-00304-6.

Watanabe, S., Hu, C., 2022. Lattice Boltzmann simulations for multiple tidal turbines using actuator line model. J. Hydrodyn. 34, 372–381. https://doi.org/10.1007/s42241-022-0037-0.

Xu, J., Wang, L., Yuan, J., Fu, Y., Wang, Z., Zhang, B., Luo, Z., Tan, A.C.C., 2025. Mesh-based data-driven approach for optimization of tidal turbine blade shape. Energy 328, 136699. https://doi.org/10.1016/J.ENERGY.2025.136699.

Zhang, Y., Liu, Z., Li, C., Wang, X., Zheng, Y., Zhang, Z., Fernandez-Rodriguez, E., Mahfoud, R.J., 2022. Fluid–Structure interaction modeling of structural loads and fatigue life analysis of tidal stream turbine. Mathematics 10, 3674. https://doi.org/10.3390/math10193674.

Zhang, Y., Zang, W., Zheng, J., Cappietti, L., Zhang, J., Zheng, Y., Fernandez-Rodriguez, E., 2021. The influence of waves propagating with the current on the wake of a tidal stream turbine. Appl. Energy 290, 116729. https://doi.org/10.1016/j.apenergy.2021.116729.